# Tunable Type-II BiVO$_4$/g-C$_3$N$_4$ Nanoheterostructures for Photocatalysis Applications

Jihua Zhang,[1] Mingsen Deng,[1] Yunan Yan,[1] Tiejun Xiao,[1] Wei Ren,[2,*] and Peihong Zhang[3,†]

[1]*Guizhou Provincial Key Laboratory of Computational Nano-Material Science, Guizhou Education University, Guiyang 550018, China*
[2]*Department of Physics, and International Center of Quantum and Molecular Structures, Materials Genome Institute, Shanghai University, Shanghai 200444, China*
[3]*Department of Physics, University at Buffalo, State University of New York, Buffalo, New York 14260, USA*

Bismuth vanadate–graphitic carbon nitride (BiVO$_4$/g-C$_3$N$_4$) heterostructures combining the advantages of bismuth vanadate and graphitic carbon nitride have recently emerged as a promising material system for photocatalytic applications. Further performance improvement will require in-depth understanding and fine tuning the near-edge electronic properties of these heterostructures. We investigate the electronic properties, in particular, the band-edge states, that control the optical and transport properties of BiVO$_4$/g-C$_3$N$_4$ nanoheterostructures using the Heyd-Scuseria-Ernzerhof (HSE) hybrid functional approach. Our results demonstrate that BiVO$_4$/g-C$_3$N$_4$ heterostructures have a desired type-II band alignment, which may greatly facilitate rapid separation of photogenerated carriers. We find that the BiVO$_4$ subsystem is responsible for the robust and strong optical absorption observed experimentally. Our calculated absorption edge of about 2.5 eV agrees remarkably well with the experimental value of 2.45 eV. We also investigate the effect of an external electric field on the band-edge states, band alignment, and the optical and fundamental band gaps of the BiVO$_4$/g-C$_3$N$_4$ heterostructures. The band-edge states of the BiVO$_4$ and g-C$_3$N$_4$ subsystems respond very differently to the applied electric field, resulting in electric field-tunable band offsets and band gap of the BiVO$_4$/g-C$_3$N$_4$ heterostructures. The contrasting response of the fundamental and optical gaps to an electric field suggests an alternative avenue for future experimental optimization of the optical absorption and carrier separation dynamics of these heterostructures for photoelectrochemical catalysis applications.

## I. INTRODUCTION

Semiconductor-based photocatalysis has received tremendous research attention in the wake of concerns about global environmental pollution and energy crisis [1]. In the past few decades, several methods [2–4] have been developed to overcome the serious shortcomings of fast charge recombination and limited visible-light absorption of semiconductor photocatalysts. One of the most widely explored strategies is the use of photocatalytic heterojunctions [2,5–7]. Previous work [8,9] has demonstrated that the construction of two semiconductors with suitable electronic structures may exhibit superior photoactivity than single photocatalysts. In particular, a type-II band alignment at the heterostructure interface can facilitate rapid separation of photogenerated electron–hole pairs, resulting in significantly improved photocatalytic performance.

Bismuth vanadate (BiVO$_4$) is one of the most promising photocatalytic materials for water oxidation [10–14] due to its moderate band gap, high optical absorption, abundance, low cost, and high stability [15–18]. On the other hand, graphite-phase carbon nitride g-C$_3$N$_4$ also exhibits good visible-light response [19,20] and has attracted a great deal of scientific interest for its applications in photocatalytic water splitting [19,21–26] and organic pollutant degradation [27–31]. Therefore, it is plausible that BiVO$_4$/g-C$_3$N$_4$ heterostructures [9,32–39], which combine the advantages of g-C$_3$N$_4$ and BiVO$_4$, might give rise to superior photocatalytic performance. Experimentally, it is found that the BiVO$_4$/g-C$_3$N$_4$ heterojunctions with different weight ratios of g-C$_3$N$_4$ result in varying photocatalytic efficiencies. For example, Kong *et al.* reported that a BiVO$_4$/g-C$_3$N$_4$ heterostructure (26.94 wt. % of BiVO$_4$) exhibits an excellent oxygen evolution rate of 750 $\mu$mol h$^{-1}$ g$^{-1}$ under visible light irradiation, which represents a 129% increase compared to that of pristine BiVO$_4$, and a photonic efficiency of 19% [40]. Che and coworkers [41] concluded that a 50:50 mass ratio BiVO$_4$/g-C$_3$N$_4$ heterojunction was

---

*renwei@shu.edu.cn
†pzhang3@buffalo.edu

the best for photocatalysis, showing remarkably higher photocatalytic activities in degrading rhodamineB (RhB) compared with pure $C_3N_4$ or $BiVO_4$. Sui and coworkers [39] demonstrated that a $BiVO_4/g$-$C_3N_4$ heterojunction with 7 wt. % g-$C_3N_4$ was seven times more efficient than pristine $BiVO_4$. On the other hand, Sun *et al.* [37] showed that a $BiVO_4/g$-$C_3N_4$ heterojunction with 3% $BiVO_4$ exhibited the highest photocatalytic efficiency. Therefore, it is clear that optimal $BiVO_4/g$-$C_3N_4$ heterostructures have not been identified and there is still much room for improving their photocatalytic efficiency.

To better understand the improved photocatalytic performance of the $BiVO_4/g$-$C_3N_4$ heterojunctions, it is important to carry out systematic studies of their electronic properties and how they may be tuned, for example, with different weight ratios of the subsystems or with an external field. Theory is able to provide useful insight for understanding experimental results and guidance for experimental design of heterostructures for improved photocatalytic performance.

Experimentally, it is difficult to realize a tunable band gap by controlling the weight ratio of g-$C_3N_4$ in the $BiVO_4/g$-$C_3N_4$ heterojunction. For example, Sui and coworkers [39] concluded that the optical band gaps of $BiVO_4$ and $BiVO_4/g$-$C_3N_4$ (with 3, 5, 7, 10 wt. % g-$C_3N_4$) are basically the same (about 2.45 eV) since they observed little change to the absorption edge among the samples. Their conclusion is consistent with several other experimental results [33,38,42]. However, it is often desirable to tune the electronic properties of heterostructures for optimal performance in different applications and conditions, and applying an electric field is one of most convenient and effective approaches. Indeed, Kan and coworkers [43] have demonstrated that the band gap of bilayer g-$C_3N_4$, and thus the optical properties, can be easily tuned by an external electric field.

In this work, we first investigate the structural and electronic properties of the $BiVO_4/g$-$C_3N_4$ heterojunctions with different numbers of g-$C_3N_4$ layers. This study provides an in-depth understanding of the important electronic structures features such as band gap, band-edge states, band alignment, and the effect of the g-$C_3N_4$ layer thickness on the electronic and structural properties of these structures. We then study the effects of the electric field on the electronic structure and interfacial properties of the $BiVO_4/g$-$C_3N_4$ heterojunctions. We find that $BiVO_4/g$-$C_3N_4$ heterojunctions have a desired type-II band alignment and that the $BiVO_4$ subsystem is responsible for the robust optical gap observed in experiments. In addition, the fundamental (minimum) band gap of the $BiVO_4/g$-$C_3N_4$ heterojunction can be effectively tuned by applying an external electric field, and a transition from semiconductor to metal is observed; the optical band gap, on the other hand, remains rather robust, but can also be tuned between 2.05 to 2.55 eV with a moderate electric field.

More interestingly, the greater the number of the g-$C_3N_4$ layers, the more effective the electric field is in tuning the band gap.

## II. COMPUTATIONAL

Density-functional-theory- (DFT) based first-principles calculations are performed using the projected augmented wave (PAW) [44] method implemented in the Vienna *ab initio* simulation package (VASP) [45,46]. The Kohn-Sham one-electron states are expanded using the plane wave basis set with a kinetic energy cutoff of 500 eV. The Perdew-Burke-Ernzerhof (PBE) [47] exchange-correlation (XC) functional within the generalized gradient approximation (GGA) is employed for the geometrical optimization. Since the van der Waals (vdW) interaction is expected to be important in these layered structures, in this work, we adopt the DFT-D3(BJ) [48] method with a Becke-Johnson- (BJ) damped [49,50] vdW correction.

Since the GGA approach usually underestimates the band gap of semiconductors, we use the screened hybrid functional of Heyd-Scuseria-Ernzerhof (HSE) [51] for a more accurate description of the electronic structure. In this work, we use the HSE06 functional [51] with a screening parameter $\omega = 0.2$ Å$^{-1}$ and a small mixing parameter $\alpha$ ($\alpha = 0.175$) for the short-range Hartree-Fock exchange instead of the commonly used value of 0.25. Using these parameters (i.e., $\omega = 0.2$ Å$^{-1}$ and $\alpha = 0.175$), the calculated band gaps of isolated monolayer g-$C_3N_4$ (2.70 eV) and bulk $BiVO_4$ (2.45 eV) compare well with experimental results (2.7 eV [22] for g-$C_3N_4$ and 2.5 eV [52] for bulk $BiVO_4$) and previous theory (2.7 eV [9,53] for g-$C_3N_4$ and 2.4 eV [54] for bulk $BiVO_4$).

We mention that one should be cautious when comparing the theoretical band gap calculated here with experiments since the measured band gap includes several renormalization effects [55,56], including (but not limited to) electron-phonon renormalization, lattice polarization, and spin-orbit coupling effects. However, accurate calculations of the quasiparticle band gaps are not the main focus of this work. We expect that the band-gap renormalization effects do not change the main results of this work since we attempt to model the already renormalized gap and band alignments, which are reproduced reasonably (admittedly fortuitously) using the HSE functional with the appropriately chosen HF mixing parameter.

The Brillouin-zone (BZ) integration is carried out using the Monkhorst-Pack [57] sampling method with a density of $2 \times 6 \times 1$ for the $BiVO_4/g$-$C_3N_4$ heterostructures. A vacuum layer of 15 Å is included to avoid interaction between neighboring slabs. The external electric field is introduced by adding a planar dipole layer in the middle of the vacuum layer in the periodic supercell [58] as implemented in VASP. The effects of the applied electric field on

the atomic structure are neglected as they are very small. All atoms are fully relaxed until the maximum magnitude of the force acting on the atoms is smaller than 0.03 eV/Å. We define the positive direction of the electric field as pointing from BiVO$_4$ (010) to g-C$_3$N$_4$, as shown in the inset of Fig. 1(f).

Note that there is substantial lattice mismatch between BiVO$_4$ and g-C$_3$N$_4$. For the heterostructures studied in this work, we use the averaged lateral lattice constants (of the supercells) to minimize the strains on both subsystems to within ±3.5%. This strain introduces a small enhancement to the band gap of the BiVO$_4$ slab from 2.45 eV to about 2.7 eV. For the g-C$_3$N$_4$ overlayer, the strain and interfacial interaction cause the structure to buckle as shown in Fig. 1. The buckling effects significantly enhance the band gap of g-C$_3$N$_4$ to about 3.1 eV, as compared with about 2.7 eV for flat g-C$_3$N$_4$.

The imaginary part $\epsilon_2(\omega)$ of the dielectric function $\epsilon(\omega)$ is calculated using the standard formulation

$$\varepsilon_2(\omega) = \frac{Ve^2}{2\pi \hbar m^2 \omega^2} \int d^3k \sum_{n,n'} | < n\vec{k}|\vec{p}|n'\vec{k} > |^2$$

$$\times f_{n\vec{k}}(1 - f_{n'\vec{k}})\delta(E_{n\vec{k}} - E_{n'\vec{k}} - \hbar\omega), \quad (1)$$

where $V$ is the cell volume, $\hbar\omega$ is the energy of the incident photon, $\vec{p}$ is the momentum operator, $|n\vec{k}>$ is the electronic state, and $f_{n\vec{k}}$ is the Fermi occupation function. The real part $\epsilon_1(\omega)$ is related to $\epsilon_2(\omega)$ by the Kramer-Krönig transformation. The absorption coefficient $a(\omega)$ can be derived from $\epsilon_1(\omega)$ and $\epsilon_2(\omega)$ as follows [59]

$$\alpha(\omega) = \frac{\sqrt{2}\omega}{c}\left[\sqrt{\varepsilon_1^2(\omega) + \varepsilon_2^2(\omega)} - \varepsilon_1(\omega)\right]^{1/2}. \quad (2)$$

## III. RESULTS AND DISCUSSION

### A. Structural properties

In order to reduce the in-plane lattice mismatch, the heterostructure models are created by placing the g-C$_3$N$_4$ layers with a $2\sqrt{3} \times 1$ supercell and different thicknesses onto a 12-layer-thick $3 \times 1$ BiVO$_4$ (010) slab. In addition, we use the averaged lattice constants of the subsystems for the heterostructure models to minimize the effects of the lattice mismatch. The bottom six layers of the BiVO$_4$ (010) slab are fixed at the bulk structure while the top six layers are allowed to relax. We will denote the single-layer, double-layer, and trilayer g-C$_3$N$_4$ on BiVO$_4$ (010) surface models as BiVO$_4$/SL-g-C$_3$N$_4$, BiVO$_4$/BL-g-C$_3$N$_4$, and BiVO$_4$/TL-g-C$_3$N$_4$, which are illustrated in Figs. 1(a), 1(c), and 1(e), respectively. We have studied several nonequivalent structures, namely, four for BiVO$_4$/SL-g-C$_3$N$_4$, eight for BiVO$_4$/BL-g-C$_3$N$_4$, and sixteen for BiVO$_4$/TL-g-C$_3$N$_4$. The lowest energy structures of BiVO$_4$/SL-g-C$_3$N$_4$, BiVO$_4$/BL-g-C$_3$N$_4$, and

BiVO$_4$/TL-g-C$_3$N$_4$ are shown in Figs. 1(b), 1(d), and 1(f), respectively. These low energy structures we found are by no means the most stable structures. However, our main results should not be affected significantly if slightly different structures are used. In the following, we will focus on these lowest energy structures. It should be pointed out that both $I2/b$ and $C2/c$ space groups are commonly used to describe the monoclinic scheelite structure of BiVO$_4$ [14]. Here, we use the $C2/c$ space group notion. The (010) surface using the $C2/c$ space group notation is equivalent to the (001) surface using the $I2/b$ notion, which has been shown to be the most stable one [60]. Ideally, theoretical studies of photocatalysis should consider surface hydration effects as adsorption of water may modify the surface electronic properties. In addition, hydration may also cause degradation of photocatalysts. The issue of hydration effects is beyond the scope of this study but definitely deserves further investigation.

In order to address the stability of the heterostructures, we define an interface adhesion energy

$$E(\text{ad}) = [E(\text{hetero})E(\text{g-C}_3\text{N}_4) - E(\text{BiVO}_4)]/S, \quad (3)$$

where $E(\text{hetero})$, $E(\text{g-C}_3\text{N}_4)$, and $E(\text{BiVO}_4)$ are the total energies of the relaxed BiVO$_4$/g-C$_3$N$_4$ heterostructure, g-C$_3$N$_4$ (001), and BiVO$_4$ (010) slabs, respectively; $S$ is the area of the interface. The calculated adhesion energies for BiVO$_4$/SL-g-C$_3$N$_4$, BiVO$_4$/BL-g-C$_3$N$_4$, and BiVO$_4$/TL-g-C$_3$N$_4$ heterostructures are $-0.20$, $-0.25$, and $-0.18$ eV/Å$^2$, respectively, suggesting that these structures are stable. These adhesion energies are consistent with those for g-C$_3$N$_4$ (001) on the Zn$_2$GeO$_4$ (110) surface ($-0.18$ eV/Å$^2$) [61] and graphene-coupled Bi$_2$WO$_6$ (010) surface ($-0.18$ eV/Å$^2$) [8]. It should be noted that the calculated adhesion energy is significantly greater than that for typical vdW systems such as graphite, suggesting that both physical and chemical effects contribute to the surface adhesion. However, chemical hybridization effects are rather weak and there are no chemical bonds formed at the interface.

After structural optimization, the g-C$_3$N$_4$ layers show considerable distortion, as shown in Figs. 1(b), 1(d), and 1(f). The structural distortions, in particular, the wavy distortion features, are due in part to the lattice mismatch, which is about 3%. The local distortions and the small interfacial distances, however, suggest significant interfacial chemical interactions at the interface, which is similar to the results for the g-C$_3$N$_4$ (001)/ZnWO$_4$ (010) heterostructure [62] and bilayer-g-C$_3$N$_4$/MoS$_2$ heterostructure [53]. We would like to mention that the lattice mismatch has minimal effects on the electronic structures. The vertical separation between the g-C$_3$N$_4$ layer and the BiVO$_4$ (010) surface is 1.85 Å [h$_1$ in Fig. 1(b)] for the BiVO$_4$/SL-g-C$_3$N$_4$ structure, 2.24 Å [h$_2$ in Fig. 1(d)] for BiVO$_4$/BL-g-C$_3$N$_4$, and 1.89 Å
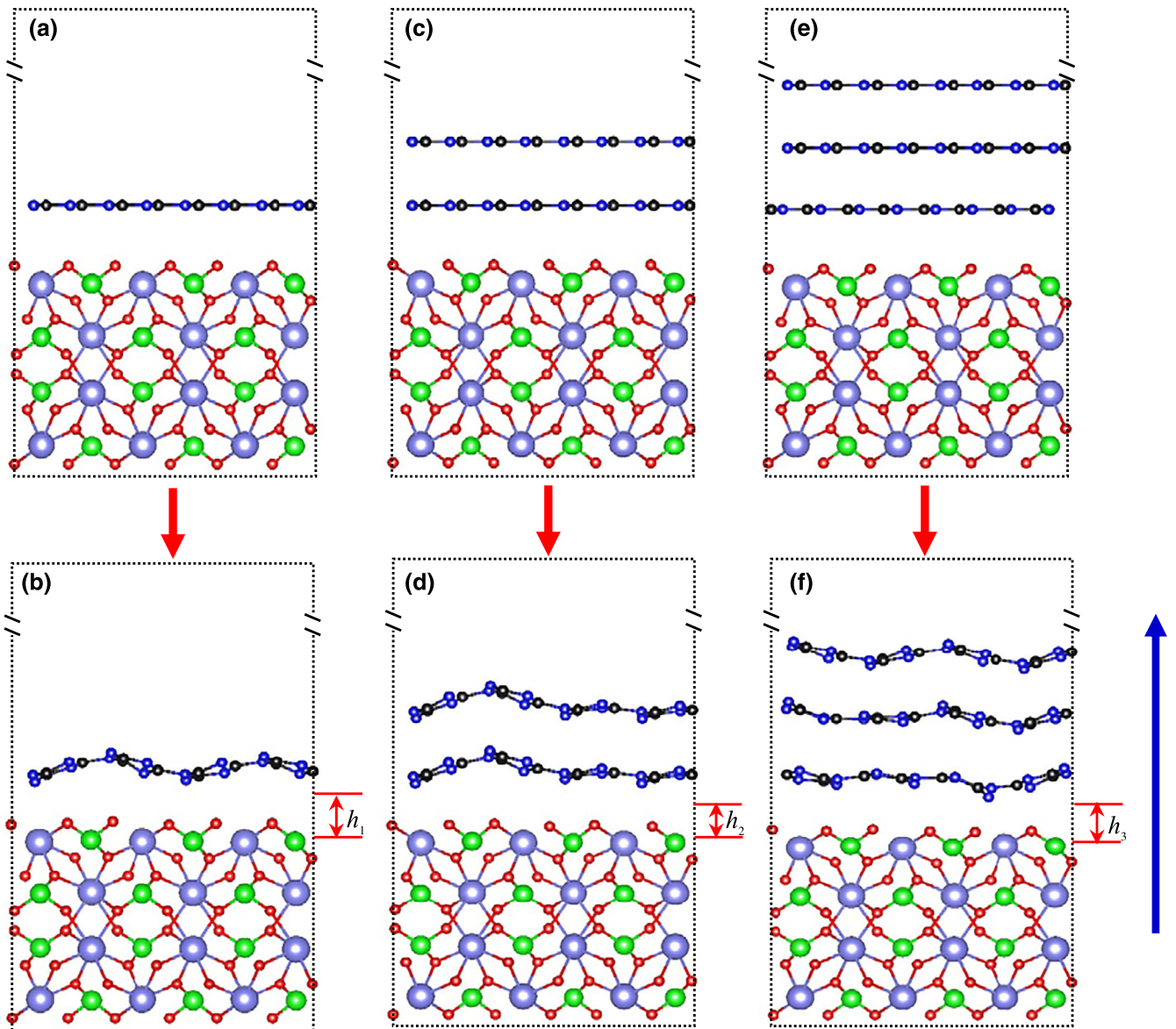
FIG. 1. Side view of the $BiVO_4$/SL-g-$C_3N_4$, $BiVO_4$/BL-g-$C_3N_4$, and $BiVO_4$/TL-g-$C_3N_4$ heterostructures: (a), (c), and (e) are structures before optimization and (b), (d), and (f) are after optimization, respectively. Red, green, light blue, blue, and black balls represent O, V, Bi, N, and C atoms, respectively. The blue arrows indicate the direction of the applied electric field.

[$h_3$ in Fig. 1(f)] for $BiVO_4$/TL-g-$C_3N_4$. These inter-layer separations are smaller than typical vdW inter-action distances. For example, the interlayer separation is 2.89 Å for the graphene/g-$C_3N_4$ heterostructure [63], 2.87 Å for g-$C_3N_4$/$TiO_2$(100) [64], and 3.16 Å for DL-g-$C_3N_4$/$MoS_2$ [53]. The shorter interlayer distance implies a stronger interlayer interaction between the $BiVO_4$ and g-$C_3N_4$ layers.

## B. Electronic structure and band alignment

Electronic structures of the $BiVO_4$/g-$C_3N_4$ heterostructures are calculated using the HSE06 screened hybrid functional method. Figure 2 shows the calculated total density of state (TDOS, shown in green in Fig. 2) of the heterostructures and the partial density of state (PDOS) for the subsystems $BiVO_4$ (shown in orange) and g-$C_3N_4$ (dark blue). The position of the valence band maximum (VBM) is placed at zero for all three heterostructures for better comparison. The calculated band gaps of the $BiVO_4$/SL-g-$C_3N_4$, $BiVO_4$/BL-g-$C_3N_4$, and $BiVO_4$/TL-g-$C_3N_4$ heterostructures are 1.27, 1.24, and 1.37 eV, respectively, indicating that the number of g-$C_3N_4$ layers has little effect on the heterojunction band gap. The calculated band gap (approximately 1.2 to 1.4 eV), however, is significantly smaller than the
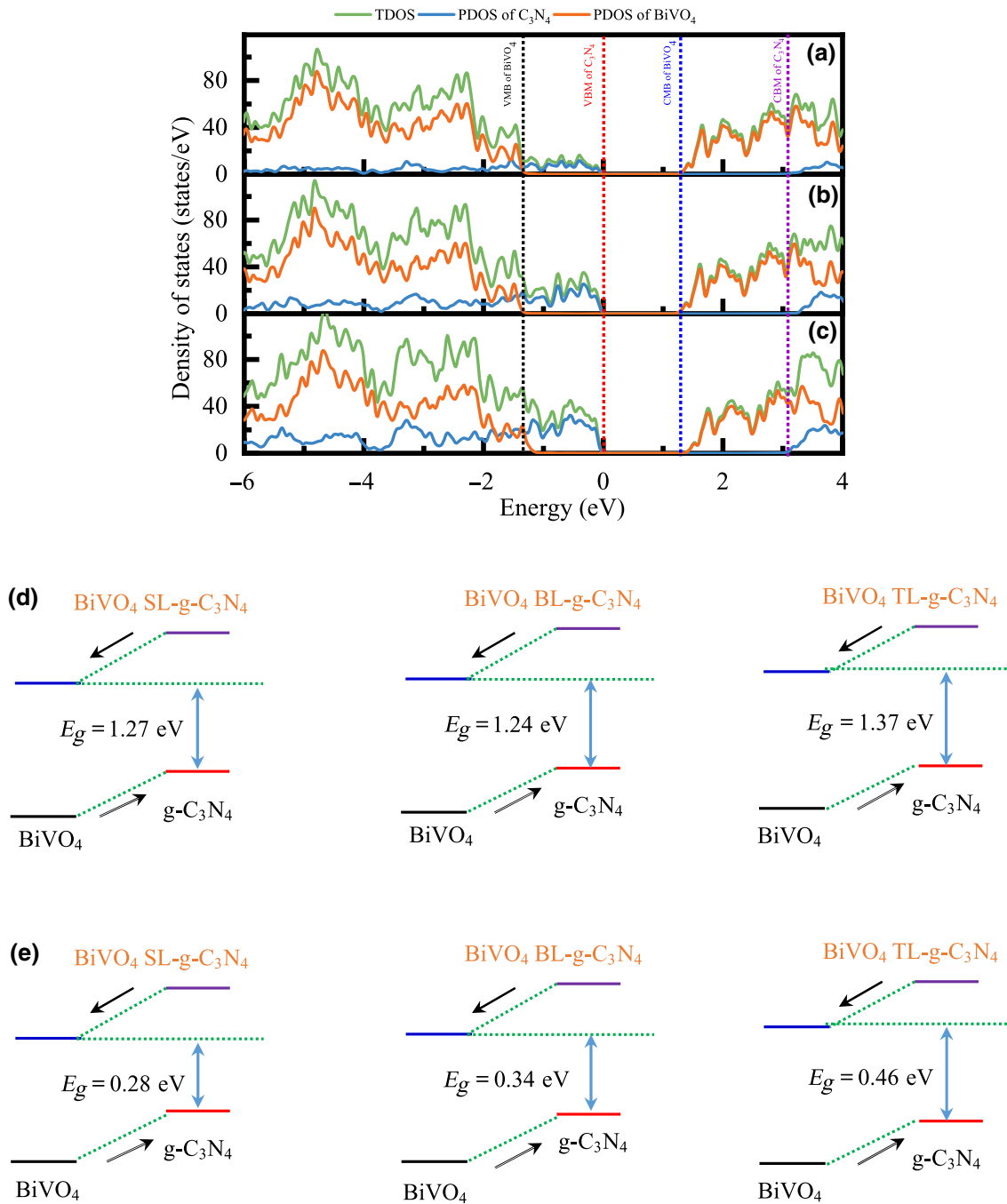
FIG. 2. Calculated TDOS and the corresponding PDOS of the C$_3$N$_4$ and BiVO$_4$ subsystems for (a) BiVO$_4$/SL-g-C$_3$N$_4$, (b) BiVO$_4$/BL-g-C$_3$N$_4$, and (c) BiVO$_4$/TL-g-C$_3$N$_4$ heterojunctions using the HSE06 functional. (d) Band alignment of the heterojunctions obtained from the PDOS analysis using the HSE06 functional. (e) Band alignment obtained using the PBE functional. Relevant electronic parameters are also given in the figure. The position of the VBM is placed at zero for easy comparison.

experimentally measured optical gap of about 2.45 eV [39]. We will address this issue in Sec. C.

Band alignment is very important in understanding the enhanced photocatalytic properties in these nanoheterojunctions since it controls the separation of photogenerated carriers, which can be conveniently obtained by plotting the partial density of states (DOS) of the subsystems across the interfaces. Dashed lines in Fig. 2 indicate the VBM and conduction band minimum (CBM) of the BiVO$_4$ and g-C$_3$N$_4$ subsystems, and the resulting band alignment diagrams are shown in Fig. 2(d). It is clear that all three heterostructures have a type-II [65,66] band alignment. Therefore, photogenerated lowest-energy electrons and holes will spontaneously separate in these structures,
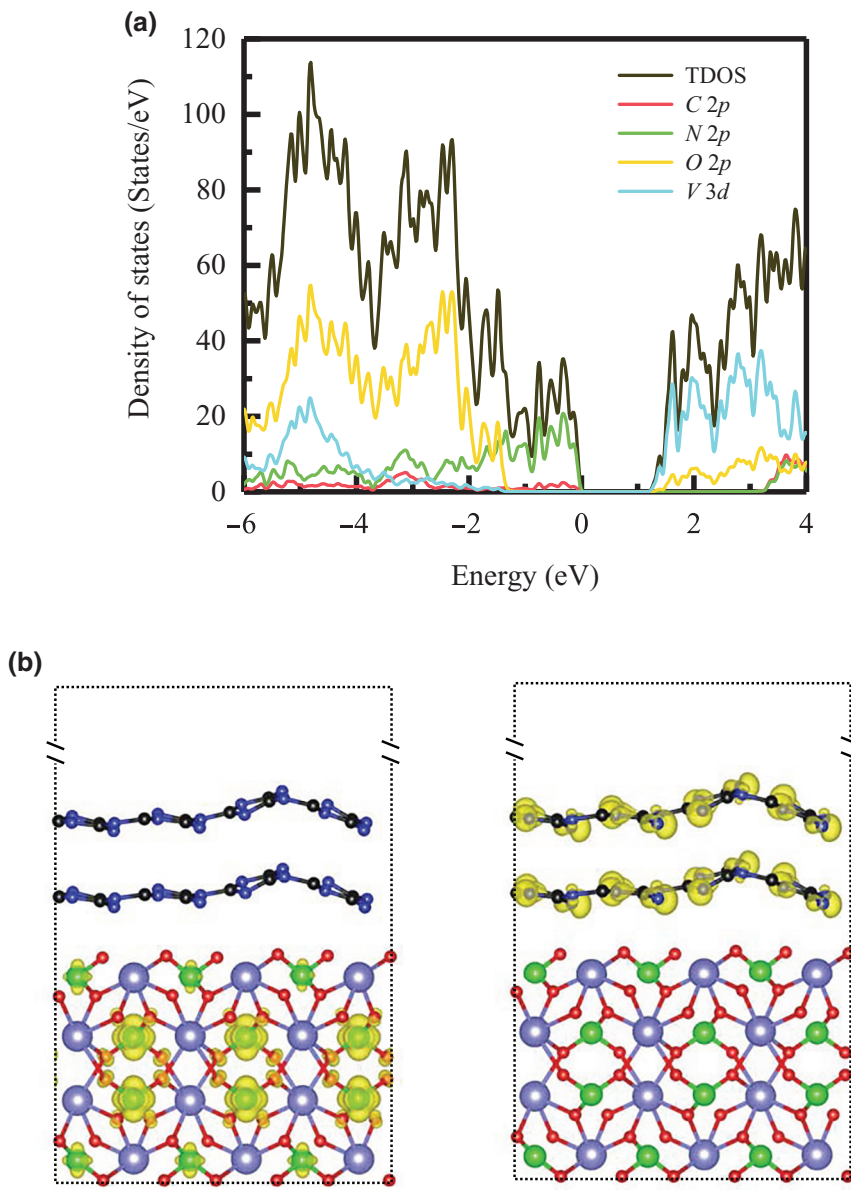
FIG. 3. (a) Calculated TDOS and atomically resolved PDOS of the BiVO$_4$/BL-g-C$_3$N$_4$ heterojunction using the HSE06 functional. Only dominant contributions from atomic states are shown in the figure. The VBM is placed at zero. (b) Isosurface charge density plots for the CBM (left panel) and VBM (right panel) in BiVO$_4$/BL-g-C$_3$N$_4$ with an isosurface value of 0.02 $e$/a.u.$^2$.

making them suitable for photocatalysis applications. Our theoretical results are consistent with experimental observations [33,34,38]. For comparison, we also show in Fig. 2(e) the band alignment diagrams calculated using the PBE functional. Although the band gaps of the heterostructures are severely underestimated with the PBE functional, the qualitative features of the band alignments are similar to those calculated using the HSE functional. We would like to mention that calculating the band alignments of bulk solids typically involves several steps due to the need to line up the electrostatic potential of the individual bulk solids [67]. For finite systems, however, band alignments at the interface can be obtained by inspecting the atomically resolved DOSs.

To gain further insight into the electronic properties of these heterostructures, we show in Fig. 3(a) atomically resolved projected DOS using BiVO$_4$/BL-g-C$_3$N$_4$ as a representative system. It is evident that the VBM state is primarily of a N$2p$ character with some contribution from C$2p$ states while the CBM is mostly of a V$3d$ character with a small admixture of O$2p$ states. A more vivid picture of these atomically (therefore, spatially) distinct characters of the VBM and CBM states is shown with the real-space charge density plot of the VBM and CBM states [Fig. 3(b)]. These results clearly reveal that the CBM and VBM states are localized in different layers of the BiVO$_4$/g-C$_3$N$_4$ heterostructures, thus facilitating the separation of electrons and holes when photocarriers are generated. As a result, the undesirable rapid electron-hole recombination can be greatly suppressed in these structures. Similar results are found for other systems by Niu *et al.* [68].
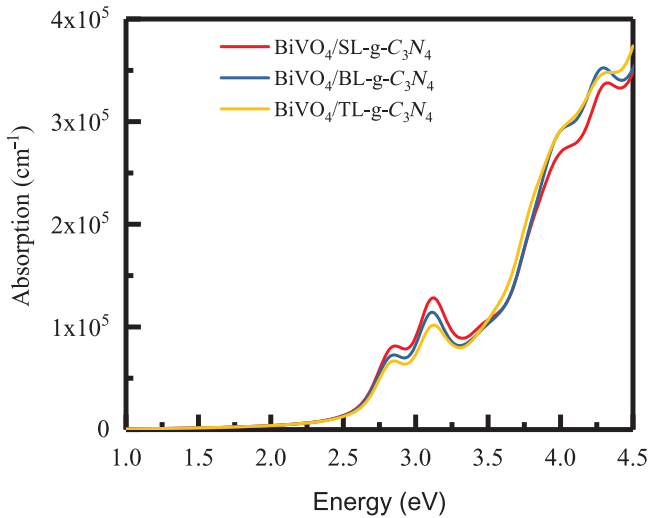
FIG. 4. Absorption coefficients of BiVO$_4$/SL-g-C$_3$N$_4$, BiVO$_4$/BL-g-C$_3$N$_4$, and BiVO$_4$/TL-g-C$_3$N$_4$ heterojunctions calculated using the HSE06 functional.

## C. Optical properties of BiVO$_4$/g-C$_3$N$_4$ heterostructures

As we mentioned earlier, the experimentally measured optical gap is about 2.45 eV for the BiVO$_4$/g-C$_3$N$_4$ heterostructures, whereas the calculated HSE minimum gap ranges from 1.2 to 1.4 eV. Therefore, there appears to be a significant discrepancy between theory and experiment. Although, in principle, the Kohn-Sham gap cannot be compared directly with the optical excitation gap, we still expect a better agreement with experimental results considering that our HSE calculations reproduce the experimental gaps for both BiVO$_4$ and g-C$_3$N$_4$ subsystems well. To this end, we carry out optical absorption calculations for the BiVO$_4$/g-C$_3$N$_4$ heterostructures at the DFT (HSE) level. Figure 4 shows the calculated optical absorption coefficient for the three heterostructures studied in this work. Interestingly, our calculations predict a sharp absorption starting at about 2.5 eV, regardless of the number of the g-C$_3$N$_4$ layers, which agrees remarkably well with the experimental result of 2.45 eV [39].

The significant difference between the calculated minimum (fundamental) band gap and the optical absorption gap can be understood with the projected DOS shown in Figs. 2 and 3. As we have discussed in the previous section, the VBM states are mostly derived from the g-C$_3$N$_4$ subsystem, whereas the CBM states are from BiVO$_4$. The optical dipole matrix elements between these spatially separated VBM and CBM states are greatly suppressed due to the minimal overlap between the initial and final state wave functions. It is evident that strong absorption occurs when the photon energy exceeds the band gap of BiVO$_4$, and the BiVO$_4$ subsystem is responsible for the optical absorption at 2.45 eV.

We would like to mention that for layered systems such as those studied here, both the quasiparticle self-energy and excitonic effects are important because of the relatively weak screening in the system. Ideally, one needs to carry out higher level calculations [69] beyond DFT to compare with optical experiments. Interestingly, it was found that the quasiparticle self-energy and the excitonic effects largely cancel out as far as the minimum absorption gap is concerned. Therefore, although the excitonic effects will strongly modify the features of the optical absorption spectrum, the overall optical band gap can be compared satisfactorily with DFT-based calculations.

## D. Tuning the band-edge states with an electric field

The robust optical gap may be considered as an advantageous property of the BiVO$_4$/g-C$_3$N$_4$ heterostructures. On the other hand, it may also be desirable that this optical gap (shown in Fig. 4) as well as the fundamental gap (shown in Fig. 2) be tunable to suit different application needs. In this regard, the nearly constant optical and fundamental gaps may become a drawback. Applying an external electric field is one of the most effective ways for tuning the electronic properties of nanostructures such as the heterostructures studied in this work.

We have investigated the effect of an external electric field on the band-edge states and the optical and fundamental band gaps of the BiVO$_4$/g-C$_3$N$_4$ heterostructures. The external electric field (**E**) is applied perpendicularly to the layer plane, which is important in practical applications [43,70,71]. We mention that we neglect the additional lattice distortions due to the applied electric field since they are found to be very small in our study. For example, with an applied field of 0.6 V/Å, additional relaxation only amounts to about a 2 meV/atom change in the calculated energy. The lack of a large permanent dipole moment of the model structure helps to explain the small structural distortion effects. The calculated permanent dipole along the direction of the applied electric field is only about 1.0 D for the whole BiVO$_4$/SL-g-C$_3$N$_4$ system. For comparison, the permanent dipole moment of a single LiF molecule is about 6.5 Debye. The evolution of the fundamental (minimum) band gap with the applied external electric field **E** for the three BiVO$_4$/g-C$_3$N$_4$ heterostructures is shown in Fig. 5. All three BiVO$_4$/g-C$_3$N$_4$ heterostructures show a similar electric field dependence on the fundamental band gap, with the band gap of the BiVO$_4$/TL-g-C$_3$N$_4$ structure showing the strongest field dependence. The band gap can be tuned between 0 and 2.1 eV with the electric field changing from −0.3 to 0.3 V/Å for the BiVO$_4$/TL-g-C$_3$N$_4$ structure. This widely tunable band gap with a moderate electric field makes these structures an ideal choice for applications where improved performance may be achieved through band-gap optimization. In addition, the electric-field-induced semiconductor-metal transition may
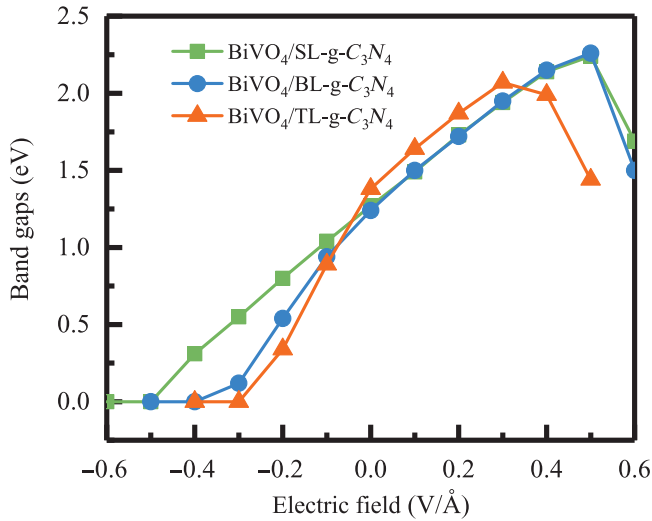
FIG. 5.   Calculated fundamental band gaps of $BiVO_4/SL$-g-$C_3N_4$, $BiVO_4/BL$-g-$C_3N_4$, and $BiVO_4/TL$-g-$C_3N_4$ heterostructures as a function of the external field.

find alternative applications for these structures beyond photocatalysis, such as switching devices.

Since the band-edge states of the $BiVO_4$ and g-$C_3N_4$ subsystems have distinct characters, we expect that they respond differently to the applied electric field. Thus, not only the fundamental band gap but also the band offsets and optical absorption gap may be tuned by an electric field. Figure 6(a) illustrates how the band-edge states of the subsystems $BiVO_4$ and g-$C_3N_4$ in the $BiVO_4/TL$-g-$C_3N_4$ structure vary with the electric field. There are a few interesting observations that deserve mentioning. Both the CBM and VBM of the $BiVO_4$ subsystem move higher with increasing electric field, indicating that the electric dipole of these states is opposite to the positive direction defined in Fig. 1. The small nonlinear behavior is a result of second-order effects. The band-edge states of the g-$C_3N_4$ subsystem, on the other hand, show a very different response to the electric field. The VBM of g-$C_3N_4$ does not shift appreciably with the electric field, indicating that this state has a negligible dipole moment. The CBM of g-$C_3N_4$, however, shows an interesting parabolic behavior around zero electric field, suggesting that second-order effects play an important role.

The different response of the subsystem band-edge states to the electric field also suggests field-tunable band offsets. Figure 6(b) shows the band gap ($E_g$), optical gap (band gap of $BiVO_4$, $E_{g\_BiVO_4}$), and the conduction and valence band offsets ($\Delta E_V$ and $\Delta E_C$) of $BiVO_4/TL$-g-$C_3N_4$ as a function of the external electric field. Both band offsets decrease monotonically with increasing **E** field, and they can both be tuned from positive to negative values. The semiconductor-metal transition is a result of the lowering of the CBM state of $BiVO_4$ with a negative electric field,
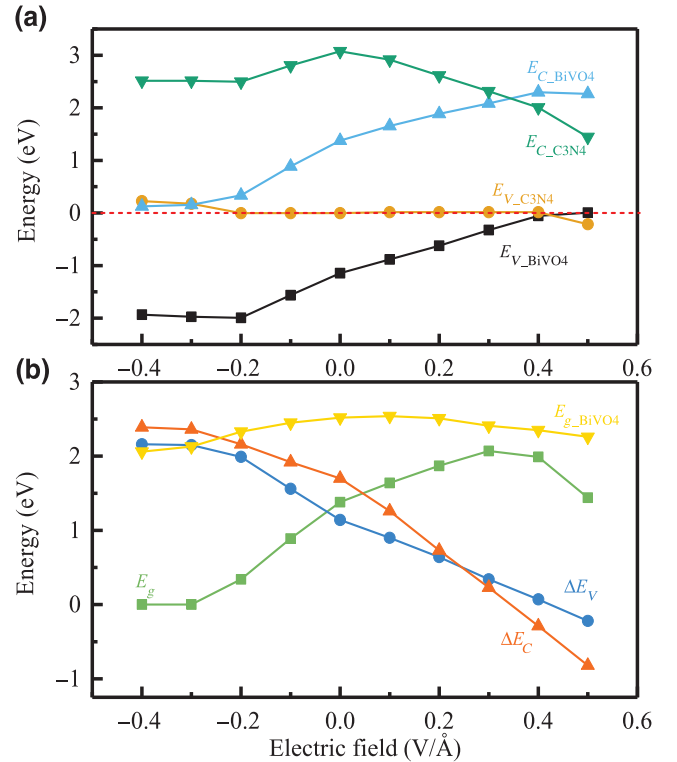


FIG. 6.   (a) Band-edge positions of the $BiVO_4$ and g-$C_3N_4$ subsystems in the $BiVO_4/TL$-g-$C_3N_4$ heterostructure as a function of the external field **E**. $E_{C\_BiVO_4}$, ($E_{C\_g\text{-}C_3N_4}$), and $E_{V\_BiVO_4}$ ($E_{V\_g\text{-}C_3N_4}$) are the CBM and VBM of $BiVO_4$ (g-$C_3N_4$) in the $BiVO_4/TL$-g-$C_3N_4$ heterostructure. The position of the VBM at zero field is place at zero. (b) Evolution of the fundamental band gap ($E_g$), optical gap of the $BiVO_4$ subsystem ($E_{g\_BiVO_4}$), and the band offsets of the $BiVO_4/TL$-g-$C_3N_4$ heterostructure as a function of the external field **E**.

which eventually merges with the VBM of the g-$C_3N_4$ subsystem. As we have shown in Fig. 4, $BiVO_4$ is mostly responsible for the optical absorption of the $BiVO_4$/g-$C_3N_4$ heterostructures. Our analysis of the electric field-dependent band-edge states also suggests that the optical band gap ($E_{g\_BiVO_4}$) of these structures can be tuned with an electric field from about 2.05 to 2.5 eV as shown in Fig. 6(b) (orange curve). Therefore, although the fundamental gap can be widely tuned from 0 to 2.1 eV with an external field changing from −0.3 to 0.3 V/Å, the optical gap remains rather robust.

## IV. SUMMARY

In summary, we carry out an in-depth analysis of the electronic properties, in particular, the band-edge states that control the optical and transport properties, of the $BiVO_4$/g-$C_3N_4$ nanoheterostructures using the HSE hybrid density-functional approach. The distinct atomic character of the band-edge states clearly indicates a type-II band alignment in these structures, which is beneficial

for the separation of photogenerated carriers. Although the fundamental gap (1.2–1.4 eV) of the BiVO$_4$/g-C$_3$N$_4$ heterostructures is considerably smaller than that of the BiVO$_4$ or g-C$_3$N$_4$ subsystems, we find that strong optical absorption starts at about 2.5 eV for all three heterostructures investigated in this work. This result agrees remarkably well with the experimental observation of robust optical absorption at 2.45 eV.

We also study the effect of an external electric field on the band-edge states, band alignment, and the optical and fundamental band gaps of the BiVO$_4$/g-C$_3$N$_4$ heterostructures. The band-edge states of the BiVO$_4$ and g-C$_3$N$_4$ subsystems respond very differently to the applied electric field, resulting in electric-field-tunable band offsets and band gap of the BiVO$_4$/g-C$_3$N$_4$ heterostructures. The fundamental gap can be widely tuned from over 2.0 eV to zero, suggesting an electric-field-induced semiconductor-metal transition in these structures. The optical gap, although it can also be tuned slightly by an electric field from 2.0 to 2.5 eV, remains rather robust. This contrasting response of the fundamental and optical gaps to an electric field may be exploited in future experiments to optimize the optical absorption and carrier separation dynamics in these heterostructures for photoelectrochemical catalysis applications.

[1] H. Tong, S. Ouyang, Y. Bi, N. Umezawa, M. Oshikiri, and J. Ye, Nano-photocatalytic materials: Possibilities and challenges, Adv. Mater. **24**, 229 (2012).

[2] K. Sivula and R. van de Krol, Semiconducting materials for photoelectrochemical energy conversion, Nat. Rev. Mater. **1**, 15010 (2016).

[3] K. Maeda, Photocatalytic water splitting using semiconductor particles: History and recent developments, J. Photochem. Photobiol. C **12**, 237 (2011).

[4] X. Chen, S. Shen, L. Guo, and S. S. Mao, Semiconductor-based photocatalytic hydrogen generation, Chem. Rev. **110**, 6503 (2010).

[5] H. Wang, L. Zhang, Z. Chen, J. Hu, S. Li, Z. Wang, J. Liu, and X. Wang, Semiconductor heterojunction photocatalysts: Design, construction, and photocatalytic performances, Chem. Soc. Rev. **43**, 5234 (2014).

[6] S. Wang, J.-H. Yun, B. Luo, T. Butburee, P. Peerakiatkhajohn, S. Thaweesak, M. Xiao, and L. Wang, Recent progress on visible light responsive heterojunctions for photocatalytic applications, J. Mater. Sci. Technol. **33**, 1 (2017).

[7] M. Bärtsch and M. Niederberger, The role of interfaces in heterostructures, ChemPlusChem **82**, 42 (2017).

[8] F. Ren, J. Zhang, Y. Wang, and W. Yao, A graphene-coupled Bi$_2$WO$_6$ nanocomposite with enhanced photocatalytic performance: A first-principles study, Phys. Chem. Chem. Phys. **18**, 14113 (2016).

[9] J. Zhang, F. Ren, M. Deng, and Y. Wang, Enhanced visible-light photocatalytic activity of a g-C$_3$N$_4$/BiVO$_4$ nanocomposite: A first-principles study, Phys. Chem. Chem. Phys. **17**, 10218 (2015).

[10] A. Kudo, K. Omori, and H. Kato, A novel aqueous process for preparation of crystal form-controlled and highly crystalline BiVO$_4$ powder from layered vanadates at room temperature and its photocatalytic and photophysical properties, J. Am. Chem. Soc. **121**, 11459 (1999).

[11] A. Kudo, K. Ueda, H. Kato, and I. Mikami, Photocatalytic O$_2$ evolution under visible light irradiation on BiVO$_4$ in aqueous AgNO$_3$ solution, Catal. Lett. **53**, 229 (1998).

[12] N. Aiga, Q. Jia, K. Watanabe, A. Kudo, T. Sugimoto, and Y. Matsumoto, Electron–phonon coupling dynamics at oxygen evolution sites of visible-light-driven photocatalyst: bismuth vanadate, J. Phys. Chem. C **117**, 9881 (2013).

[13] H. W. Jeong, T. H. Jeon, J. S. Jang, W. Choi, and H. Park, Strategic modification of BiVO$_4$ for improving photoelectrochemical water oxidation performance, J. Phys. Chem. C **117**, 9104 (2013).

[14] Y. Park, K. J. McDonald, and K. S. Choi, Progress in bismuth vanadate photoanodes for use in solar water oxidation, Chem. Soc. Rev. **42**, 2321 (2013).

[15] Z. F. Huang, L. Pan, J. J. Zou, X. Zhang, and L. Wang, Nanostructured bismuth vanadate-based materials for solar-energy-driven water oxidation: A review on recent progress, Nanoscale **6**, 14044 (2014).

[16] F. F. Abdi, N. Firet, and R. van de Krol, Efficient BiVO$_4$ thin film photoanodes modified with cobalt phosphate catalyst and W-doping, ChemCatChem **5**, 490 (2013).

[17] M. S. Prévot and K. Sivula, Photoelectrochemical tandem cells for solar water splitting, J. Phys. Chem. C **117**, 17879 (2013).

[18] P. Bornoz, F. F. Abdi, S. D. Tilley, B. Dam, R. van de Krol, M. Graetzel, and K. Sivula, A bismuth vanadate–cuprous oxide tandem cell for overall solar water splitting, J. Phys. Chem. C **118**, 16959 (2014).

[19] A. Thomas, A. Fischer, F. Goettmann, M. Antonietti, J.-O. Müller, R. Schlögl, and J. M. Carlsson, Graphitic carbon nitride materials: Variation of structure and morphology and their use as metal-free catalysts, J. Mater. Chem. **18**, 4893 (2008).

[20] W. J. Ong, L. L. Tan, Y. H. Ng, S. T. Yong, and S. P. Chai, Graphitic carbon nitride (g-C$_3$N$_4$)-based photocatalysts for artificial photosynthesis and environmental remediation: Are we a step closer to achieving sustainability?, Chem. Rev. **116**, 7159 (2016).

[21] X. Wang, K. Maeda, X. Chen, K. Takanabe, K. Domen, Y. Hou, X. Fu, and M. Antonietti, Polymer semiconductors

for artificial photosynthesis: Hydrogen evolution by mesoporous graphitic carbon nitride with visible light, J. Am. Chem. Soc. **131**, 1680 (2009).

[22] X. Wang, K. Maeda, A. Thomas, K. Takanabe, G. Xin, J. M. Carlsson, K. Domen, and M. Antonietti, A metal-free polymeric photocatalyst for hydrogen production from water under visible light, Nat. Mater. **8**, 76 (2009).

[23] J. Hong, X. Xia, Y. Wang, and R. Xu, Mesoporous carbon nitride with in situ sulfur doping for enhanced photocatalytic hydrogen evolution from water under visible light, J. Mater. Chem. **22**, 15006 (2012).

[24] K. Takanabe, K. Kamata, X. Wang, M. Antonietti, J. Kubota, and K. Domen, Photocatalytic hydrogen evolution on dye-sensitized mesoporous carbon nitride photocatalyst with magnesium phthalocyanine, Phys. Chem. Chem. Phys. **12**, 13020 (2010).

[25] H. Yan, Y. Chen, and S. Xu, Synthesis of graphitic carbon nitride by directly heating sulfuric acid treated melamine for enhanced photocatalytic $H_2$ production from water under visible light, Int. J. Hydrogen Energy **37**, 125 (2012).

[26] K. Maeda, X. Wang, Y. Nishihara, D. Lu, M. Antonietti, and K. Domen, Photocatalytic activities of graphitic carbon nitride powder for water reduction and oxidation under visible light, J. Phys. Chem. C **113**, 4940 (2009).

[27] P. Niu, G. Liu, and H.-M. Cheng, Nitrogen vacancy-promoted photocatalytic activity of graphitic carbon nitride, J. Phys. Chem. C **116**, 11013 (2012).

[28] J. Li, B. Shen, Z. Hong, B. Lin, B. Gao, and Y. Chen, A facile approach to synthesize novel oxygen-doped g-$C_3N_4$ with superior visible-light photoreactivity, Chem. Commun. **48**, 12017 (2012).

[29] Y. Cui, Z. Ding, P. Liu, M. Antonietti, X. Fu, and X. Wang, Metal-free activation of $H_2O_2$ by g-$C_3N_4$ under visible light irradiation for the degradation of organic pollutants, Phys. Chem. Chem. Phys. **14**, 1455 (2012).

[30] S. C. Yan, Z. S. Li, and Z. G. Zou, Photodegradation of rhodamine B and methyl orange over boron-doped g-$C_3N_4$ under visible light irradiation, Langmuir **26**, 3894 (2010).

[31] S. C. Yan, Z. S. Li, and Z. G. Zou, Photodegradation performance of g-$C_3N_4$ fabricated by directly heating melamine, Langmuir **25**, 10397 (2009).

[32] D. Jiang, L. Chen, J. Zhu, M. Chen, W. Shi, and J. Xie, Novel p-n heterojunction photocatalyst constructed by porous graphite-like $C_3N_4$ and nanostructured BiOI: Facile synthesis and enhanced photocatalytic activity, Dalton Trans. **42**, 15726 (2013).

[33] C. Li, S. Wang, T. Wang, Y. Wei, P. Zhang, and J. Gong, Monoclinic porous $BiVO_4$ networks decorated by discrete g-$C_3N_4$ nano-islands with tunable coverage for highly efficient photocatalysis, Small **10**, 2783 (2014).

[34] J. Su, Z. Bai, B. Huang, X. Quan, and G. Chen, Unique three dimensional architecture using a metal-free semiconductor cross-linked bismuth vanadate for efficient photoelectrochemical water oxidation, Nano Energy **24**, 148 (2016).

[35] F. Chen, Q. Yang, Y. Wang, J. Zhao, D. Wang, X. Li, Z. Guo, H. Wang, Y. Deng, C. Niu, and G. Zeng, Novel

ternary heterojunction photcocatalyst of Ag nanoparticles and g-$C_3N_4$ nanosheets co-modified $BiVO_4$ for wider spectrum visible-light photocatalytic degradation of refractory pollutant, Appl. Catal. B **205**, 133 (2017).

[36] J. Cheng, X. Yan, Q. Mo, B. Liu, J. Wang, X. Yang, and L. Li, Facile synthesis of g-$C_3N_4$/$BiVO_4$ heterojunctions with enhanced visible light photocatalytic performance, Ceram. Int. **43**, 301 (2017).

[37] R. Sun, Q. Shi, M. Zhang, L. Xie, J. Chen, X. Yang, M. Chen, and W. Zhao, Enhanced photocatalytic oxidation of toluene with a coral-like direct Z-scheme $BiVO_4$/g-$C_3N_4$ photocatalyst, J. Alloys Compd. **714**, 619 (2017).

[38] Y. Wang, J. Sun, J. Li, and X. Zhao, Electrospinning preparation of nanostructured g-$C_3N_4$/$BiVO_4$ composite films with an enhanced photoelectrochemical performance, Langmuir **33**, 4694 (2017).

[39] Z. Zhang, M. Wang, W. Cui, and H. Sui, Synthesis and characterization of a core–shell $BiVO_4$@g-$C_3N_4$ photo-catalyst with enhanced photocatalytic activity under visible light irradiation, RSC Adv. **7**, 8167 (2017).

[40] H. J. Kong, D. H. Won, J. Kim, and S. I. Woo, Sulfur-doped g-$C_3N_4$/$BiVO_4$ composite photocatalyst for water oxidation under visible light, Chem. Mater. **28**, 1318 (2016).

[41] F. Guo, W. Shi, X. Lin, and G. Che, Hydrothermal synthesis of graphitic carbon nitride–$BiVO_4$ composites with enhanced visible light photocatalytic activities and the mechanism study, J. Phys. Chem. Solids **75**, 1217 (2014).

[42] N. Tian, H. Huang, Y. He, Y. Guo, T. Zhang, and Y. Zhang, Mediator-free direct Z-scheme photocatalytic system: $BiVO_4$/g-$C_3N_4$ organic-inorganic hybrid photocatalyst with highly efficient visible-light-induced photocatalytic activity, Dalton Trans. **44**, 4297 (2015).

[43] F. Wu, Y. Liu, G. Yu, D. Shen, Y. Wang, and E. Kan, Visible-light-absorption in graphitic $C_3N_4$ bilayer: Enhanced by interlayer coupling, J. Phys. Chem. Lett. **3**, 3330 (2012).

[44] G. Kresse and D. Joubert, From ultrasoft pseudopotentials to the projector augmented-wave method, Phys. Rev. B **59**, 1758 (1999).

[45] G. Kresse and J. Hafner, Ab initio molecular dynamics for liquid metals, Phys. Rev. B **47**, 558 (1993).

[46] G. Kresse and J. Furthmuller, Efficient iterative schemes for ab initio total-energy calculations using a plane-wave basis set, Phys. Rev. B **54**, 11169 (1996).

[47] J. P. Perdew, K. Burke, and M. Ernzerhof, Generalized Gradient Approximation Made Simple, Phys. Rev. Lett. **77**, 3865 (1996).

[48] S. Grimme, S. Ehrlich, and L. Goerigk, Effect of the damping function in dispersion corrected density functional theory, J. Comput. Chem. **32**, 1456 (2011).

[49] E. R. Johnson and A. D. Becke, A post-Hartree-Fock model of intermolecular interactions: Inclusion of higher-order corrections, J. Chem. Phys. **124**, 174104 (2006).

[50] A. D. Becke and E. R. Johnson, Exchange-hole dipole moment and the dispersion interaction, J. Chem. Phys. **122**, 154104 (2005).

[51] J. Heyd, G. E. Scuseria, and M. Ernzerhof, Hybrid functionals based on a screened Coulomb potential, J. Chem. Phys. **118**, 8207 (2003).

[52] J. K. Cooper, S. Gul, F. M. Toma, L. Chen, Y.-S. Liu, J. Guo, J. W. Ager, J. Yano, and I. D. Sharp, Indirect bandgap and optical properties of monoclinic bismuth vanadate, J. Phys. Chem. C **119**, 2969 (2015).

[53] J. Wang, Z. Guan, J. Huang, Q. Li, and J. Yang, Enhanced photocatalytic mechanism for the hybrid g-C$_3$N$_4$/MoS$_2$ nanocomposite, J. Mater. Chem. A **2**, 7960 (2014).

[54] L. Zhang, M.-G. Ju, and W. Liang, Structural characteristics and photoinduced carrier behaviors of the mixed-phase BiVO$_4$: A first-principles theoretical study, Theor. Chem. Acc. **135**, 134 (2016).

[55] J. Wiktor, I. Reshetnyak, F. Ambrosio, and A. Pasquarello, Comprehensive modeling of the band gap and absorption spectrum of BiVO$_4$, Phys. Rev. Mater. **1**, 022401(R) (2017).

[56] J. Wiktor, F. Ambrosio, and A. Pasquarello, Role of polarons in water splitting: The case of BiVO$_4$, ACS Energy Lett. **3**, 1693 (2018).

[57] H. J. Monkhorst and J. D. Pack, Special points for brillouin-zone integrations, Phys. Rev. B **13**, 5188 (1976).

[58] J. Neugebauer and M. Scheffler, Adsorbate-substrate and Adsorbate-adsorbate Interactions of Na and K Adlayers on Al(111), Phys. Rev. B **46**, 16067 (1992).

[59] S. Saha, T. P. Sinha, and A. Mookerjee, Electronic structure, chemical bonding, and optical properties of paraelectric BaTiO$_3$, Phys. Rev. B **62**, 8828 (2000).

[60] G.-L. Li, First-principles investigation of the surface properties of fergusonite-type monoclinic BiVO$_4$ photocatalyst, RSC Adv. **7**, 9130 (2017).

[61] L. Sun, Y. Qi, C. J. Jia, Z. Jin, and W. Fan, Enhanced visible-light photocatalytic activity of g-C$_3$N$_4$/Zn$_2$GeO$_4$ heterojunctions with effective interfaces based on band match, Nanoscale **6**, 2649 (2014).

[62] L. Sun, X. Zhao, C.-J. Jia, Y. Zhou, X. Cheng, P. Li, L. Liu, and W. Fan, Enhanced visible-light photocatalytic activity of g-C$_3$N$_4$–ZnWO$_4$ by fabricating a heterojunction: investigation based on experimental and theoretical studies, J. Mater. Chem. **22**, 23428 (2012).

[63] X. Li, Y. Dai, Y. Ma, S. Han, and B. Huang, Graphene/g-C$_3$N$_4$ bilayer: Considerable band gap opening and effective band structure engineering, Phys. Chem. Chem. Phys. **16**, 4230 (2014).

[64] J. Liu, B. Cheng, and J. Yu, A new understanding of the photocatalytic mechanism of the direct Z-scheme g-C$_3$N$_4$/TiO$_2$ heterostructure, Phys. Chem. Chem. Phys. **18**, 31175 (2016).

[65] R. Marschall, Semiconductor composites: Strategies for enhancing charge carrier separation to improve photocatalytic activity, Adv. Funct. Mater. **24**, 2421 (2014).

[66] S. N. F. M. Nasir, H. Ullah, M. Ebadi, A. A. Tahir, J. S. Sagu, and M. A. Mat Teridi, New insights into Se/BiVO$_4$ heterostructure for photoelectrochemical water splitting: A combined experimental and DFT study, J. Phys. Chem. C **121**, 6218 (2017).

[67] C. G. Van de Walle and R. M. Martin, Theoretical study of band offsets at semiconductor interfaces, Phys. Rev. B **35**, 8154 (1987).

[68] X. Niu, Y. Li, H. Shu, X. Yao, and J. Wang, Efficient carrier separation in graphitic zinc oxide and blue phosphorus van der Waals heterostructure, J. Phys. Chem. C **121**, 3648 (2017).

[69] D. Y. Qiu, F. H. da Jornada, and S. G. Louie, Environmental screening effects in 2D materials: Renormalization of the bandgap, electronic structure, and optical spectra of few-layer black phosphorus, Nano Lett. **17**, 4706 (2017).

[70] Q. Sun, G. Qin, Y. Ma, W. Wang, P. Li, A. Du, and Z. Li, Electric field controlled CO$_2$ capture and CO$_2$/N$_2$ separation on MoS$_2$ monolayers, Nanoscale **9**, 19 (2017).

[71] J. Gao, G. Zhang, and Y. W. Zhang, Vastly enhancing the chemical stability of phosphorene by employing an electric field, Nanoscale **9**, 4219 (2017).